Article

Pairwise Model Potential and DFT Study of Li^+Ne_n Clusters (n = 1−20): The Structural, Electronic, and Thermodynamic Properties

Nesrine Mabrouk, Jamila Dhiflaoui,* Mohamed Bejaoui, Samah Saidi, and Hamid Berriche*

ACCESS | 📊 Metrics & More | 📖 Article Recommendations

ABSTRACT: The structural properties, relative stabilities, electronic, and thermodynamic properties, of Li^+Ne_n (n = 1−20) clusters have been studied based on a pairwise model and density functional theory (DFT) methods. In the pairwise method, the potential energy surface considered interactions between Li^+Ne, $Ne - Ne$, and many-body term. For the DFT calculations, the $B3LYP$ functional combined with the $6−311 + + G$ $(2d,2p)$ basis sets has been employed. In both methods, the Li^+Ne_6 cluster demonstrated high stability with an octahedral structure, where the Li^+ cation was surrounded by Ne atoms. Thus, the octahedral Li^+Ne_6 structure was considered to be the core for larger cluster sizes. Relative stabilities were assessed based on binding energies, second-order differences of energies, transition dipole moment, and HOMO−LUMO energy gaps. Furthermore, thermodynamic properties were calculated, revealing that the formation process of Li^+Ne_n clusters is endothermic and nonspontaneous.
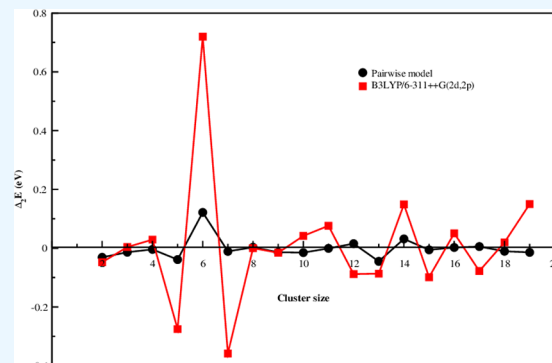
INTRODUCTION

The chemistry of ionic species assumes particular prominence in various contexts. Within the interstellar medium, extremely high-energy particles (e.g., protons) can disrupt chemical bonds or ionize species through direct collisions.[1] Conversely, within earth upper atmosphere, ionization processes may result from ion−molecule collisions, but the predominant factors are likely ultraviolet radiation and the influx of electrons and protons from the sun.[2] In contrast, the lower atmosphere of our planet primarily experiences ionization due to galactic cosmic rays (particularly in the stratosphere), natural radio-activity (e.g., alpha radiation emitted by ^{222}Rn), and γ rays originating from soil and rocks.[3] Furthermore, ion−molecule chain reactions can lead to the formation of small ion clusters[4,5] with sufficiently long lifetimes (i.e., ∼1 min in the lower atmosphere). These clusters facilitate the growth of aggregates through ion-induced nucleation, ultimately leading to the production of charged aerosols.[6−9]

Moreover, charged clusters serve as a vital link connecting isolated gas-phase ions to solvated ions in solution, offering valuable insights into the solvation phenomena. On another front, ions within plasmas play pivotal roles in the creation of nanoparticles[10,11] and polymerization processes.[12] Further-more, the identification of neutral radical species through mass spectrometry in plasmas proves effective when employing the Li+-attachment ionization method,[13] as demonstrated in the study of fluorocarbon macromolecule growth in the down-stream region of Ar/c-C_4F_8 plasmas.[14]

The gas-phase ion chemistry of noble gases, in general, and the interactions between metallic cations and rare-gas atoms, in particular, have undergone extensive theoretical and exper-imental investigations.[15−17] These interactions are primarily governed by electrostatic forces involving the ion and the induced dipole in the rare-gas, depending primarily on the polarizability of the rare-gas as well as the charge and radius of the ion.

Numerous experimental[18−27] and theoretical[28−37] inves-tigations have focused on the gas-phase ion chemistry of noble gases, particularly the interaction between metallic cations and rare-gas atoms. The dominant factor in this interaction is the electrostatic forces between the ion and the induced dipole in the rare gas. Consequently, the polarizability of the rare gas as well as the charge and radius of the ion plays a crucial role in determining the nature of this interaction.

On the experimental side, the rapid development in molecular beam techniques, combined with laser evaporation techniques, has permitted the production of clusters for almost every element in the periodic table as well as mixed clusters. The alkali ions solvated in rare gas atoms are detected by using

time-of-flight (TOF) mass spectrometry. The intensity distribution of the spectrum reflects the stability of the clusters. The distribution often exhibits an irregular size dependence, and a few stronger peaks are found at specific sizes rather than neighboring sizes. This indicates that the clusters of those particular sizes are more stable than the others. The cluster sizes corresponding to such stable structures are referred to as magic numbers. The sequences of the magic numbers found in the mass spectra serve as fingerprints of the shell closure of geometric or electronic structures or both. Therefore, the observed sequences of magic numbers provide information about the geometric and electronic structures of the clusters and thus on the interaction potential among the constituents of the clusters.

Lüder and co-workers[18] have performed time-of-flight experiments to determine the mass spectra of clusters formed by a metal ion (i.e., In^+, Al^+, and Na^+) and rare-gas. Specifically, for Na^+Ar_n, the experimental results[18] indicate the presence of clusters with a particular stable icosahedral structure for n = 6, 8, 10, 13, 16, 20, 23, 25, 26, and 29 (the so-called "magic numbers"). In contrast, the clusters where the ionic radius is significantly less than the rare-gas atomic radius lead to a new series of magic numbers that will convert into the icosahedral number for high values of n.

While determining the structure of clusters can be challenging through experimental means, it is primarily inferred from the analysis of cluster properties such as stability and spectroscopy (both vibrational and electronic). Theoretical studies, on the other hand, offer a direct means to ascertain geometries and associated stabilities while also enabling the simulation of cluster properties such as spectroscopy, dynamics, and thermodynamics. Among these theoretical approaches, ab initio calculations stand out as the preferred methods for investigating van der Waals interactions. These calculations can be based on perturbative methods such as MP2 or MP4, or they can utilize more advanced coupled-cluster (CC) approaches.

Ab initio calculations, whether based on perturbative methods such as MP2 or MP4 or employing coupled-cluster (CC) approaches, are the methods of choice for investigating van der Waals molecular clusters. These methods have the ability to incorporate dispersion forces for small clusters. However, it is important to note that when dealing with large ones they can be computationally demanding, often requiring substantial computational time.

The solvation of Li^+ with molecular solvents has been addressed by various methods,[28−30,39−55,57−60] while similar studies involving rare-gas atoms are scarce in the literature. However, Froudakis et al.[20] have performed mass spectra experiments on Li^+Ne_n, Li^+Ar_n, and Li^+Kr_n clusters. Additionally, they have also carried out MP2 calculations for the small size Li^+Ne_n and Li^+Ar_n clusters, while molecular dynamics quenching minimization has been used for the larger Li^+Ar_n structures. It is apparent from this work[20] that magic numbers arise for n = 4 and n = 6 irrespective of the rare-gas atom, and n = 34 for clusters with argon or krypton as solvents; less pronounced, but always reproducible peaks appear in the mass spectra at n = 14 and 16 for all systems.

Recently, the low energy configurations of Li^+Ar_n (n = 2−10) clusters have been optimized by Prudente et al.[38] using the MP_2 method with a quadruple-ζ basis set. They found good agreement with those reported by Boatz et al.[36] Later, alkali metals in helium matrices were investigated by Marinetti et

al.,[47] employing a combination of classical energy minimization techniques and an exact quantum diffusion Monte Carlo (DMC) method.

More recently, Ben Hadj Ayed et al.[48] have studied the structure and stability of Na^+Ne_n using the DFT level of theory and the pairwise method. In such work, the authors fitted the numerical potential of Ahlrichs et al.[85] data for Na^+Ne to obtain new analytic potentials. Furthermore, they have used the basin-hopping method[75−77] to locate the putative global minima of Na^+Ne_n (n = 1−16) clusters and confirmed the preference of positive metal ions to occupy a position in the center of the cluster when solvated with rare-gas atoms.[48] The structural properties and relative stabilities of the Na^+Ne_n clusters, with n = 1−16, have been reoptimized by density functional theory (DFT) methods combined with the augmented $aug − cc − pVTZ$ basis sets. For both methods, the high stability is obtained for Na^+Ne_{12} cluster with an icosahedral structure, and the 12 Ne atoms complete the first solvation shell around the Na^+ cation.

In the present study, we want to investigate the structure, relative stability, and electronic and thermodynamic properties of the Li^+Ne_n clusters. To achieve this aim, we have performed ab initio calculations for Li^+Ne and Ne_2, which allows for the construction of a new analytical potential surface for the Li^+Ne_n clusters that include many-body (V_{3B}) interaction. The methodology followed in this work is detailed in section II, where we also describe the pairwise potential model and DFT calculations employed for the global geometry optimization of clusters. In section III, we present the structure for Li^+Ne_n and discuss the relative stabilities and electronic and thermodynamic properties. Finally, the main conclusions are summarized in section 4.

II. COMPUTATIONAL METHODS

II.1. Pairwise Method. In this study, we constructed an analytical potential energy surface (PES) for the Li^+Ne_n clusters. The developed PES incorporates various components, including the core−core interaction energy ($V_{Li^+Ne}(R_i)$), the interactions between Ne atoms ($V_{Ne−Ne}(r_{ij})$), and the many-body term (V_{3B}). These components are combined in the following summation:

$$V_{tot} = \sum_{i=1}^{n} V_{Li^+Ne}(R_i) + \sum_{j=1}^{n} \sum_{i<j}^{n} V_{Ne−Ne}(r_{ij}) + V_{3B}$$

To model the analytical Li^+Ne_n PES, we have performed coupled cluster calculations including single and double excitations plus triple excitations calculated with perturbation theory $CCSD(T)$ for the Li^+Ne and $Ne − Ne$ diatomic species in their ground electronic states. All these single-point calculations have been carried out with the Molpro,[60] using the $aug − cc − pVn$ (n = D, T, Q,5, and 6) Z basis set[56] for both Li and Ne atoms.

Moreover, all the ab initio energies have been extrapolated to the complete basis set (CBS) limit using a two-parameter expression,[57−59] applied to the total energy as follows: $E_n = E_{CBS} + \frac{A}{n^3}$. Here, n = 4 and 5 correspond to the AVQZ and AV5Z basis sets, respectively. E_n represents the computed total energy corresponding to the specific basis set, E_{CBS} is the CBS extrapolated energy, and A is a fitting parameter. The energies obtained from the AVQZ and AV5Z basis set calculations were used for the extrapolation process.

Table 1. Spectroscopy Parameters for Li^+Ne and $Ne-Ne$ Using the $CCSD\ (T)$ Method and the $aug-cc-pVn$ ($n = Q, 5$ and 6) Z Basis Sets and CBS Extrapolation

method and basis sets (Li/Ne)	R_e(Å)	D_e(cm^{-1})	ω_e(cm^{-1})	$\omega_e\chi_e$(cm^{-1})	B_e(cm^{-1})	references
Li^+Ne						
$CCSD(T)/AVDZ$	2.131	829.97	196.02	11.57	0.718853	this work
$CCSD(T)/AVTZ$	2.088	951.84	212.55	11.86	0.748766	this work
$CCSD(T)/AVQZ$	2.062	979.26	225.28	12.95	0.767024	this work
$CCSD(T)/AV5Z$	2.064	983.76	224.64	12.82	0.766281	this work
$CCSD(T)/CBS[Q5]$	2.066	988.46	224.35	12.73	0.764865	this work
mobilities	2.07	989.83	229.00	14.7		61
scattering	2.110	1065.24				62
EXRHF3	2.045	1000.96				64
$CCSD(T) + CP$	2.064	1006.89				70
$Ne - Ne$						
$CCSD(T)/AV5Z$	3.099	30.16	28.51	6.73	0.173968	this work
$CCSD(T)/AV6Z$	3.102	28.62	27.79	6.74	0.173634	this work
$CCSD(T)/CBS\ [56]$	3.105	26.50	26.94	6.84	0.173272	this work
exp	3.091	28.5	28.5			67
fitting	3.098	28.62				69
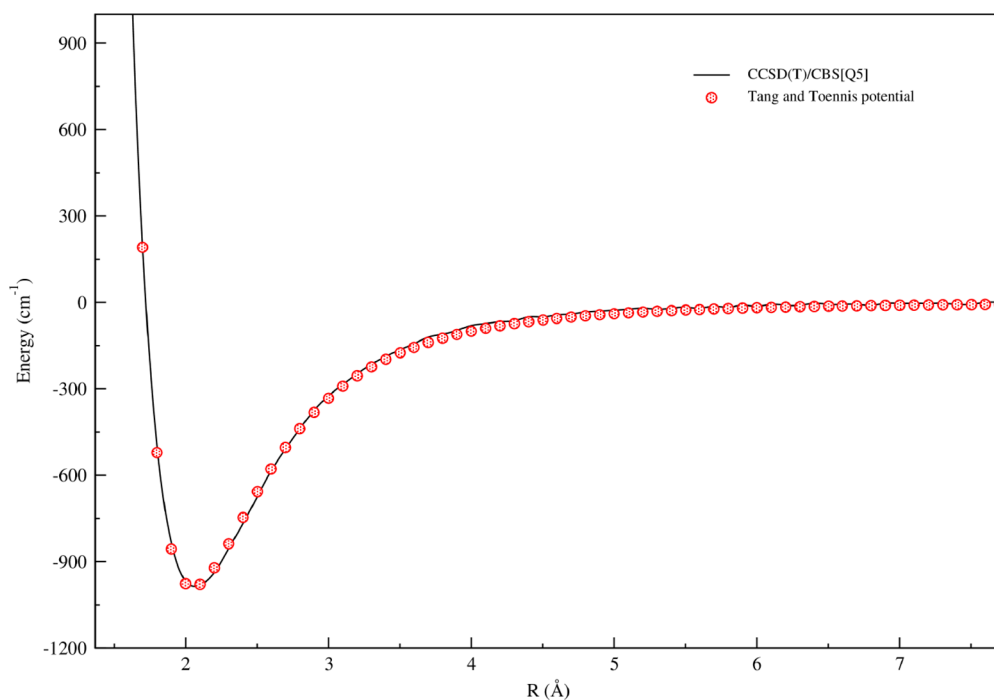
Figure 1. Potential energy curves for the Li^+Ne interaction: $CCSD(T)/CBS[Q5]$ ab initio calculation and Tang and Toennies (TT) analytical potential.

The calculated spectroscopic parameters for the Li$^+$Ne and Ne − Ne using the $CCSD\ (T)$ method and different bases are summarized in Table 1 and compared with available theoretical[62,64,69,70] and experimental work.[61,63,65−67] From Table 1, it can be observed that our values for the X$^1\Sigma^+$ states for Li$^+$Ne and Ne − Ne dimers can be considered in excellent agreement with the experimental values.[61,67] The calculated potential curves of the ground states of the Li$^+$Ne and Ne − Ne systems have a minimum of 988.46 and 28.62 cm^{-1} situated at 2.066 and 3.102 Å, respectively, whereas a well of 989.83 cm^{-1} is observed at 2.07 Å for Li$^+$Ne and 28.5 cm^{-1} at 3.091 Å for Ne − Ne dimer by the experimental work.[61,67] However, comparing our results of Li$^+$Ne and Ne − Ne systems to the theoretical results,[62,64,69,70] we observe a good agreement.

In order to achieve accurate interactions within Li^+Ne_n clusters, we employ a standard least-square fit procedure to interpolate the $CCSD(T)/CBS[Q5]$ numerical potentials for Li$^+$Ne and $CCSD(T)/AV6Z$ for Ne − Ne.

For Li$^+$Ne, the $CCSD(T)/CBS[Q5]$ numerical potential was fitted by using the Tang and Toennies (TT)[68] analytical form. In the (TT) model, we added a short-range repulsive Born−Mayer potential Ae^{-bR} (with A = 66.1408 hartree and b = 2.49829 a_0^{-1}) to a long-range attractive potential $\frac{C_6}{R^6} - \frac{C_8}{R^8} - \frac{C_{10}}{R^{10}}$ (with C_6 = 8.77624 a_0^6, C_8 = 13.5153 a_0^8, and C_{10} = −102.028 a_0^{10}), along with the polarization contribution: $-\frac{1}{2}\frac{\alpha_{Ne}}{R^4}$ (with α_{Ne} = 2.664a_0^3).[70] For the Ne − Ne interaction, the Lennard-Jones (LJ)[71] model potential is utilized as follows:

$$V_{(LJ)}(R) = 4\varepsilon\left[\left(\frac{\sigma}{R}\right)^{12} - \left(\frac{\sigma}{R}\right)^6\right]$$
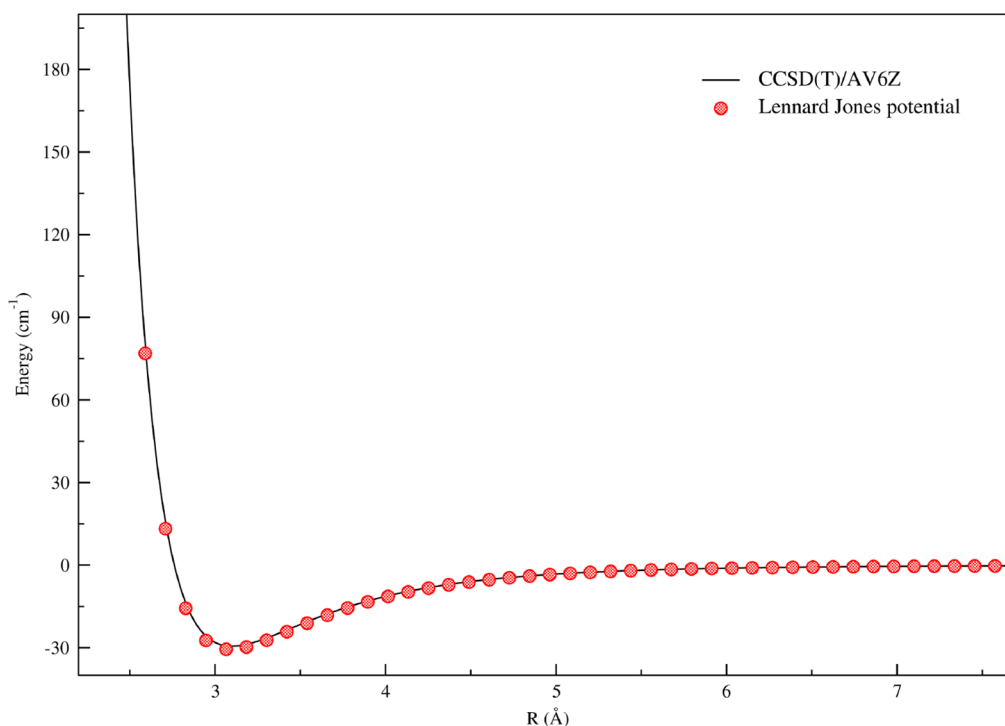
Figure 2. Potential energy curves for the $Ne - Ne$ interaction: $CCSD(T)/aug - cc - PV6Z$ ab initio calculation and Lennard-Jones (LJ) analytical potential.

where ε and σ represent, respectively, the well depth and the equilibrium distance of the Ne_2. These quantities are $\varepsilon = 1.3340210^{-4}$ hartree and $\sigma = 5.212 a_0$.

Figures 1 and 2 present a comparison of the (TT) and (LJ) analytical potentials with the $CCSD(T)/CBS[Q5]$ and $CCSD(T)/AV6Z$ energies for Li^+Ne and $Ne - Ne$, respectively. The findings depicted in these figures provide clear evidence that both the (TT) and the (LJ) analytical potentials effectively reproduce the energies computed using ab initio methods. To assess the accuracy of our fitting process, we calculated the root-mean-square (RMS) error[72,73] using the following expression: $\sqrt{\frac{\sum_{k=1}^{N_p}(V_k^{fit} - V_k^{ab-initio})^2}{N_p}}$, where N_p, represents the number of ab initio points. V_k^{fit} and $V_k^{ab-initio}$ correspond to the analytical and numerical potentials, respectively. The (TT) and (LJ) potentials yield reasonable RMS values of 2.25×10^{-5} and 7.88×10^{-6} cm^{-1}, respectively.

The final term in the total energy, denoted as V_{3B}, accounts for the many-body effects.[74] In this study, we employed the expression introduced in ref 74. to incorporate this contribution. The expression can be written as follows:

$$V_{3B} = -\alpha^2 \begin{bmatrix} \frac{3r_j}{4}g_3(r_i)g_5(r_{ij}) + \frac{3r_i}{4}g_3(r_j)g_5(r_{ij}) \\ -\frac{1}{4}g_3(r_i)g_3(r_j)g_1(r_{ij}) - \frac{3}{2}g_1(r_i)g_1(r_j)g_5(r_{ij}) \\ -\frac{1}{2}g_1(r_i)g_3(r_j)g_3(r_{ij}) - \frac{1}{2}g_3(r_i)g_1(r_j)g_3(r_{ij}) \end{bmatrix}$$

where $\alpha = 2.664\ a_0^{3}$[70] represents the polarizability of Ne, the r_i and r_j are the $Ne - Li^+$ distances, and r_{ij} represents the $Ne - Ne$ distance. Moreover, $g_n(r_i)$ is defined as $g_n(r_i) = \frac{f_n(r_i)}{r_i^n}$, where $f_n(r_i)$ corresponds to the damping function described in ref 74:

$f_n(r_i) = 1 - \exp(-br_i)\sum_{k=0}^{n}\frac{(br_i)^k}{k!}$, with b taking the values of $2.3751 a_0^{-1}$ and $2.44785\ a_0^{-1}$ for the Li^+Ne and $Ne - Ne$ interaction, respectively.

The basin-hopping global optimization method developed by Wales and Doye[75-77] was employed for the geometry optimization process. This algorithm has demonstrated remarkable efficiency, allowing for the discovery of global minima and other low-lying minima, even in challenging scenarios. The basin-hopping approach involves transforming the potential energy surface into a sequence of terraces by quenching structures generated through extensive Monte Carlo moves using local minimization. At any given point $\mathbf{R}$ in the configuration space, the energy corresponds to that of the nearest local minimum obtained through a local optimization initiated from that specific point. The transformed energy can be expressed as $\check{V}(R) = min_l V(R)$. Here, R represents a vector representing a point in the configuration space, and min_l denotes the outcome of the local minimization. By employing Monte Carlo sampling on-the-fly with the transformed potential energy surface, the anticipated global minimum can be obtained. For each cluster size n, random displacements of all atoms were attempted with a magnitude of $7.5 a_0$. The basin-hopping simulation was conducted at a temperature of 100 K. Each run involved attempting 10^5 Monte Carlo steps, accompanied by conjugate gradient local minimizations.

II.2. DFT Calculations. The DFT calculations are considered powerful tools for studying the structural and electronic properties of molecular clusters. The most stable geometries of the Li^+Ne_n ($n = 1-20$) clusters have been fully optimized using (DFT) theory and we have chosen the B3LYP functional, which incorporates Becke's exchange and Lee–Yang–Parr correlations and the $6-311 + + G(2d,2p)$) basis set. All calculations are performed using the Gaussian 09 program[79] and Avogadro as a visualization package.

Before optimization, we employed a basin-hopping approach to search for the lowest-energy structures of Li^+Ne_n $(n = 1-20)$ clusters.

In order to determine the reliability of our DFT calculations, some test calculations are carried out on Li^+Ne and $Ne - Ne$ dimers, employing various methods, including M062X/6-311, MP2, B3PW91, B3P86, and B3LYP along with different basis sets. The calculated Li^+Ne and $Ne - Ne$ bond lengths and available experimental data are listed in Table 2. It is evident that when compared to these other methods, the B3LYP method combined with the $6-311 + + G(2d,2p)$ basis set accurately reproduces the Li^+Ne_n clusters.

Table 2. Bond Length (R) of the Li^+Ne and $Ne - Ne$ Dimers[a]

methods/basis sets	$R(Li^+Ne)$	$R(Ne - Ne)$
$B3LYP/6-311+ + G(d, p)$	2.0967	3.2089
$B3LYP/6-311+ + G(d)$	2.0967	3.2099
$B3LYP/6-31+ + G(d)$	2.1086	3.2159
$B3LYP/6-311G$	2.0433	2.6743
$B3LYP/6-311+ + G(2d, 2p)$	2.0612	3.2000
$M062X -311+ + G(2d, 2p)$	2.0911	3.0859
$MP2/6-311+ + G(2d, 2p)$	2.0868	3.2225
$BLYP/6-311+ + G(2d, 2p)$	2.0873	3.3806
$B3PW91/6-311+ + G(2d, 2p)$	2.1388	3.6374
$B3P86/6-311+ + G(2d, 2p)$	2.1183	3.8924
$M06HF/6-311+ + G(2d, 2p)$	2.0907	2.8302
experimental values	2.0761	3.10067

[a]All values are in Å.

III. RESULTS AND DISCUSSION

III.1. Geometric Structure. The low-lying energy structures of Li^+Ne_n $(n = 2-20)$ clusters were calculated using both the pairwise model and the $DFT/B3LYP - 6-311 + + G(2d,2p)$ method in order to determine the global minimum structures. The Li^+Ne and $Ne - Ne$ bond lengths in each cluster are regrouped in Table 3. For the Li^+Ne dimer, Li^+ and Ne are distant by 2.058 and 2.061 Å for the pairwise and DFT methods, respectively. We may observe that, in the pairwise model and DFT results, the Li^+Ne and $Ne - Ne$ bond lengths of Li^+-Ne_n are similar to some little discrepancies. We must also mention that the distance values for the Li^+-Ne and $Ne - Ne$ tend to increase after the DFT reoptimization compared to the pairwise model results.

To see the difference between the pair model structure and DFT structure, we have computed a root-mean-square distance (RMSD) using the following expression:[80]

$$RMSD = \sqrt{\frac{1}{n} \sum_i (x_{iA} - x_{iB})^2 + (y_{iA} - y_{iB})^2 + (z_{iA} - z_{iB})^2}$$

The RMSD between the two structures, A and B, is calculated as the root-mean-square difference of their respective x, y, and z coordinates.

Figure 3 illustrates the optimized geometries obtained from these calculations. For $n = 2$, it is worth noting that the lowest-energy structures of the Li^+Ne_2 clusters obtained through both pairwise and $DFT/B3LYP$ methods exhibit notable feature. The coordination of the second Ne to Li^+ results in the formation of a linear D_∞ complex, as depicted in Figures 3 and 4. In this linear geometry, the characteristics of the Li^+Ne bond are nearly identical to those observed in the Li^+Ne dimer. This implies that the bond stabilization through covalent forces surpasses the potential energetic gain resulting from the $Ne - Ne$ attraction.

The structures obtained for Li^+Ne_3 using the pairwise method and $DFT/B3LYP$ exhibit a pyramidal arrangement, with the Li^+ ion positioned at the summit. All three R (Li^+Ne) distances are measured at 2.06 Å, while the $Ne - Ne$ bonds differ from each other and exhibit behavior similar to that of Li^+Rg_3 (Rg = He, Kr, and Xe) clusters.[78] It is worth mentioning that the equilibrium bond distances, R (Li^+Ne) and R $(Ne - Ne)$, are shorter than those of R (Li^+Xe) and R $(Xe - Xe)$ dimers, yet longer than those of (Li^+He) and R $(He - He)$ dimers. This observation can be attributed to the higher polarizability of xenon $(\alpha_{Xe} = 27.66 \ a_0^3)^{78}$ and the lower polarizability of helium $(\alpha_{He} = 1.38a_0^{378})$ compared to the neon atom $(\alpha_{Ne} = 2.664 \ a_0^3 \ [70])$.

From $n = 3$ to $n = 6$, it is important to note that the structure of the Li^+Ne_n clusters remain unchanged when examined using both pairwise and DFT methods, indicating a consistent growth pattern around the lithium cation.

The Li^+Ne_4 cation adopts a highly symmetrical tetrahedral structure. The bond between Li^+ and Ne is slightly longer compared to the bonds observed in smaller clusters. Furthermore, in smaller clusters ranging from $n = 2$ to 4, the $Ne - Ne$ distances are considerably longer compared to the bond length in the Ne_2 dimer. This suggests that interligand

Table 3. Structural Parameters (in Å) of the Li^+Ne_n Clusters Obtained Using the Pairwise Model and Density Functional Theory (DFT) Methods

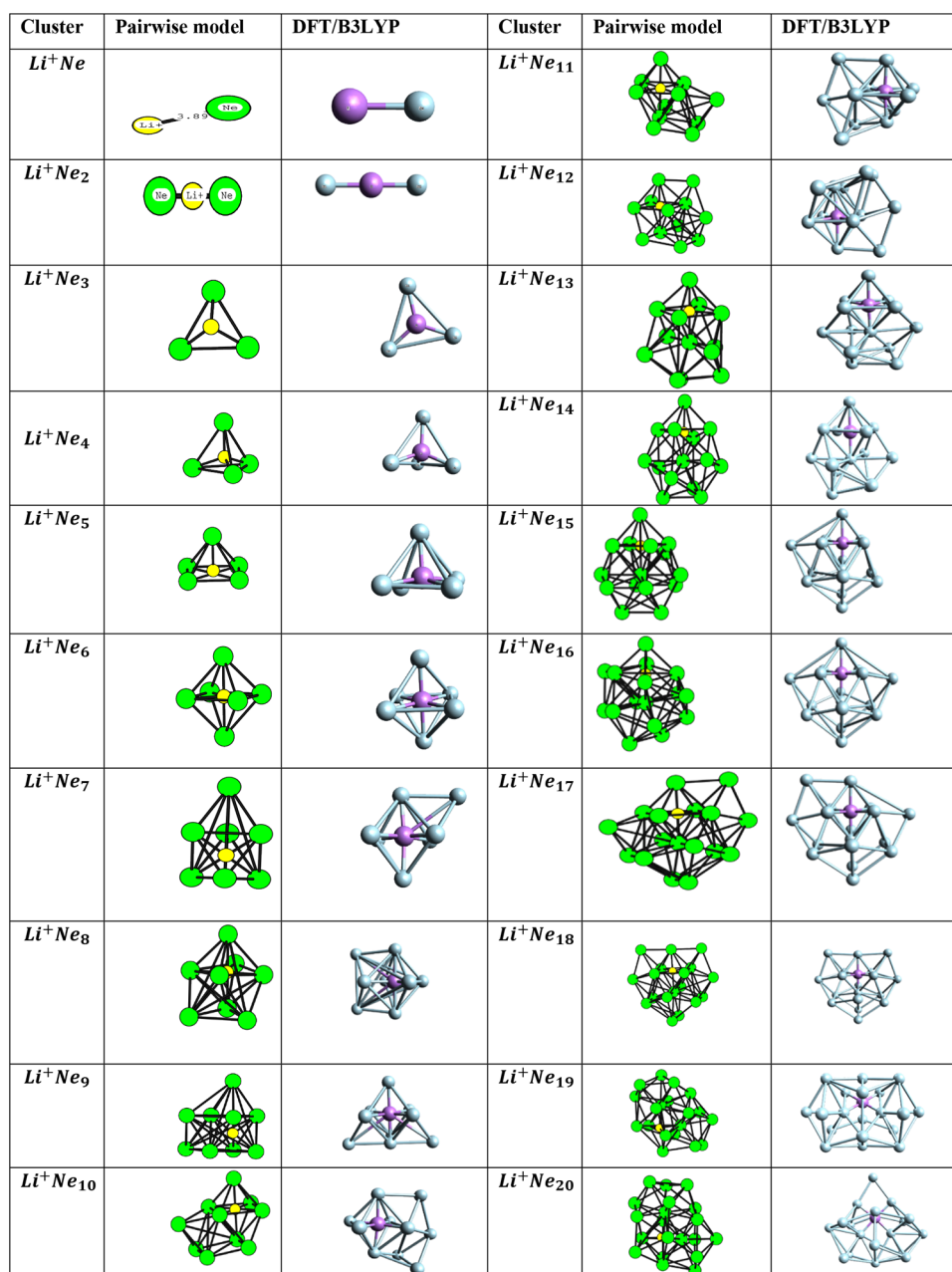| n	symmetry	pairwise model R (Li^+Ne)	pairwise model R $(Ne - Ne)$	DFT R (Li^+Ne)	DFT R $(Ne - Ne)$	RMSD
1	$C_{\infty v}$	2.058		2.061		1.219
2	$D_{\infty h}$	2.058	3.122	2.038	4.075	0.932
3	C_{3v}	2.058	3.122	2.072	3.951, 3.299	1.069
4	T_d	2.010	3.283	2.084	3.404	1.715
5	C_{4v}	2.078, 2.128	2.999, 3.097, 4.242	2.112, 2.129	4.238, 3.137, 2.968	0.262
6	O_h	2.147	3.037, 4.295	2.164	3.061, 4.332, 3.059	0.365
7	C_s	2.138, 2.156, 3.736	3.033, 3.055, 4.294	2.157	3.092, 3.053, 4.330, 5.317	0.437
8		2.129, 2.192, 3.635	2.976, 3.017, 3.376, 4.258, 4.975	2.192, 2.133, 3.638	2.973, 3.019, 3.074, 4.982, 5.331,	0.943
9		2.122, 2.156, 3.677	3.048, 3.122, 4.166, 4.298, 5.295	2.157, 2.187, 3.738	3.064, 3.138, 4.197, 4.332, 5.337,	0.173
10		2.137, 2.148, 2.168,	3.022, 3.041, 3.065, 3.097, 4.289, 4.357, 4.953, 5.309	2.171, 2.144, 3.731	3.033, 3.085, 3.114, 4.359, 5.292	1.062

Figure 3. Global minimum structures for Li^+Ne_n clusters ($n = 2-20$) determined using the pairwise model potential and the $B3LYP/6-311 + + G$ $(2d,2p)$ level of theory.

interactions play a relatively minor role in the formation of these structures.

The Li^+Ne_5 cluster exhibits a highly symmetric configuration with C_{4v} symmetry, where four neon atoms form a square shape, and an additional atom is positioned along the C_4 axis. With the addition of another neon atom to the Li^+Ne_5 cluster, the Li^+Ne_6 cluster demonstrates a very stable cluster corresponding to an octahedral geometry (square bipyramid) with an O_h symmetry, with the Li ion located at the center. In this cluster, the neon atoms are located at 2.15 Å from the central lithium ion. We again note that in this size range optimization tends to maximize the number of Li^+Ne and $Ne - Ne$ interactions at optimal distances in the first solvation shell. Moreover, in the Li^+Ne_5 and Li^+Ne_6 clusters, the Li^+Ne bond distances increase due to the reduction in ligand–ligand contacts. The two largest clusters, Li^+Ne_5 and Li^+Ne_6, are

notably influenced by $Ne - Ne$ interactions as a consequence of limited space around the central metal cation. The Li^+Ne_7, Li^+Ne_8, Li^+Ne_9, Li^+Ne_{10} conformer preserves the core structure of Li^+Ne_6 by adding respectively one, two, and three neon atoms on these faces.

For $n \geq 10$, the structures of Li^+Ne_n differ from the Li^+Ne_n complexes formed with n values ranging from 2 to 6. In the case of Li^+Ne_n ($n = 2-6$) complexes, they exhibit a distinctive arrangement with two shells: one consisting of 2 neon atoms, which are formed as two distinguished shells (2 + 5) leading to shell closing for 7 neon atoms. However, in the lowest-energy structures of Li^+Ne_n clusters for $n \geq 10$, the formation pattern continues to revolve around a square bipyramid geometry. It can be observed that the neon atoms progressively cover the lithium cation, resulting in a decrease in the attractive effects of $Ne - Ne$ interactions.
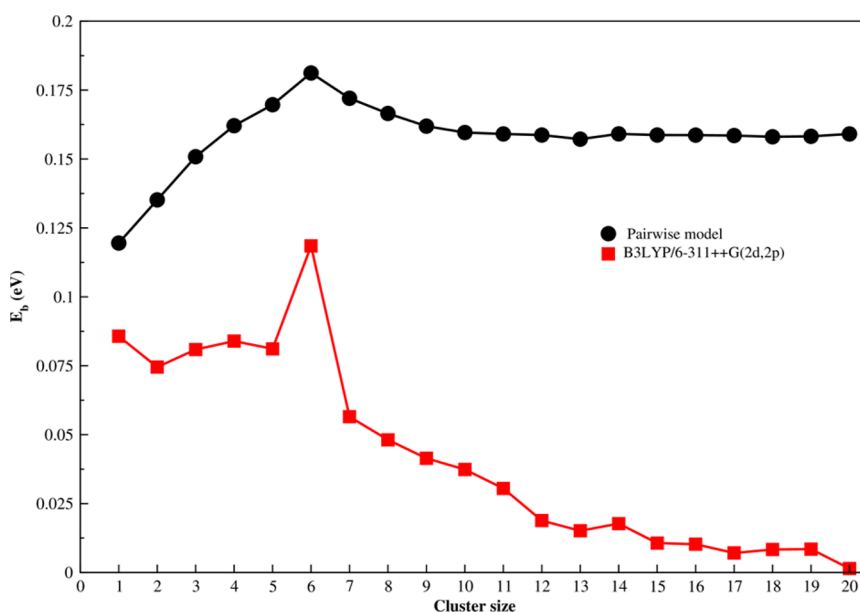
Figure 4. Size dependence of the binding energy $e_b(n)$ of the lowest energy structures for Li^+Ne_n clusters using the pairwise model potential and the $B3LYP/6-311 + + G\ (2d,2p)$ level of theory.
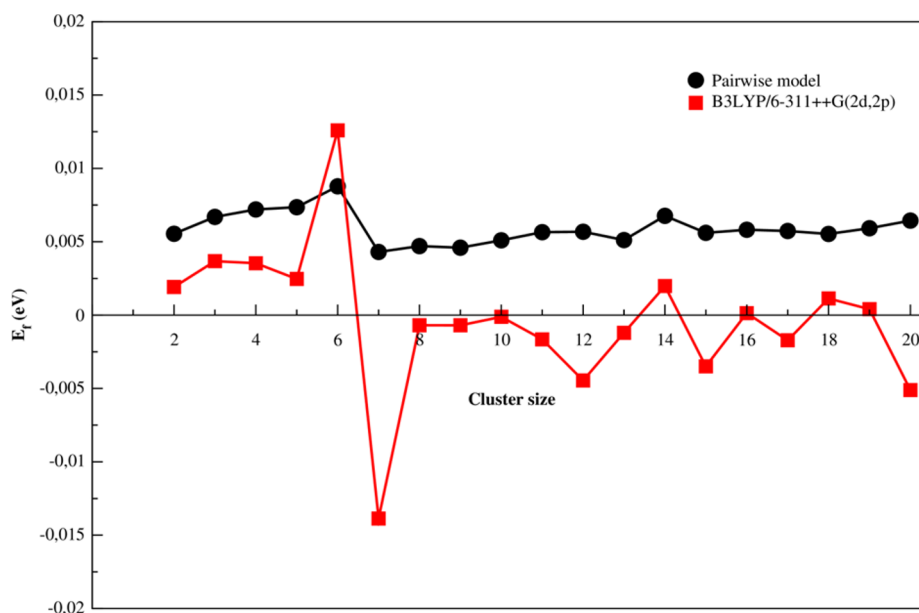

Figure 5. Size dependence of the fragmentation energy $e_f(n)$ of the lowest-energy structures for Li^+Ne_n clusters using the pairwise model potential and the $B3LYP/6-311 + + G\ (2d,2p)$ level of theory.

III.2. Relative Stabilities.

The prediction of relative stability in clusters of different sizes, such as Li^+Ne_n, can be accomplished by calculating the averaged binding energies $e_b(n)$, fragmentation energies $E_f(n)$, and second-order difference of energies $\Delta_2E(n)$; these quantities are defined by the following formulas:

$$e_b(n) = \frac{[nE(Ne) + E(Li^+) - E(Li^+Ne_n)]}{n + 1}$$

$$E_f(n) = E(Li^+Ne_{n-1}) + E(Ne) - E(Li^+Ne_n)$$

$$\Delta_2E(n) = -2E(Li^+Ne_n) + E(Li^+Ne_{n+1}) + E(Li^+Ne_{n-1})$$

where $E(Li^+Ne_{n-1})$, $E(Ne)$, $E(Li^+Ne_n)$, and $\mathrm{E}(Li^+Ne_{n+1})$ denote the total energy of the Li^+Ne_{n-1}, Ne, Li^+Ne_n, and Li^+Ne_{n+1} clusters, respectively.

Equations 5 and 6 display the calculated values of $e_b(n)$, $E_f(n)$, and $\Delta_2E(n)$ for the lowest-energy Li^+Ne_n ($n = 1-20$) clusters employing both pairwise model and DFT calculations. First, the graphs representing the averaged binding energies for both the pairwise model and DFT method exhibit a similar trend that depends on the cluster size. Second, the $e_b(n)$ values obtained from the pairwise model are larger than those from the DFT calculation. Additionally, when $n = 6$, a distinct peak is observed, indicating that Li^+Ne_6 clusters are relatively more stable than their neighboring clusters. Moreover, the averaged binding energy progressively decreases as the cluster size
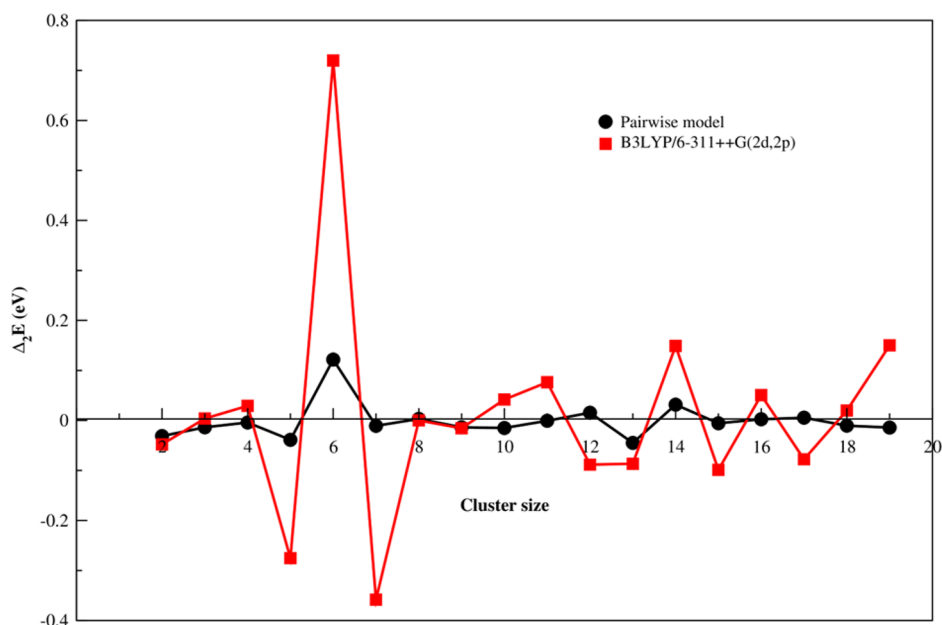
Figure 6. Size dependence of the second order energy difference $\Delta_2E(n)$ of the lowest-energy structures for Li^+Ne_n clusters using the pairwise model potential and the $B3LYP/6-311 + + G\ (2d,2p)$ level of theory.
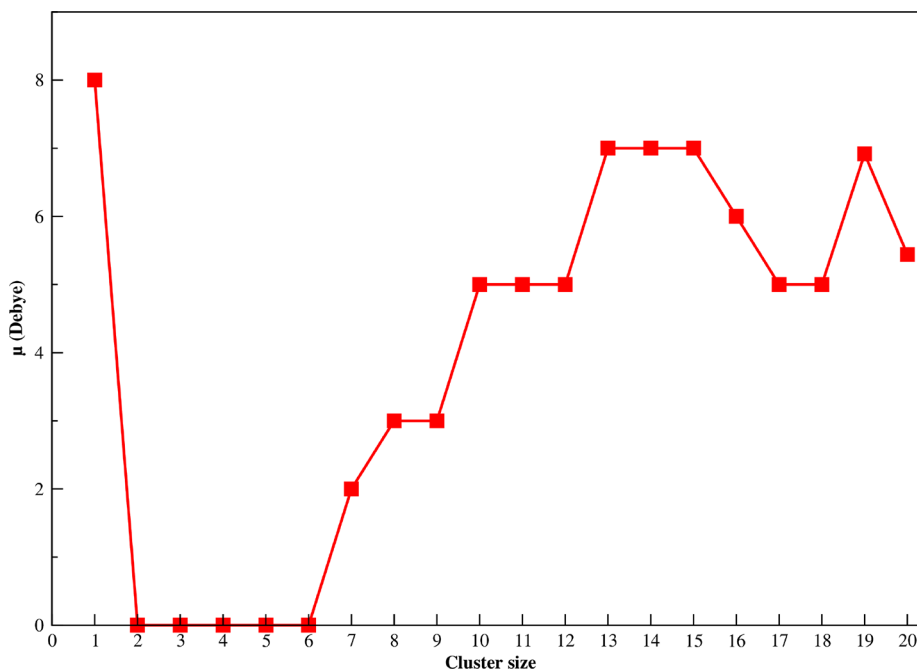
Figure 7. Dipole moment of Li^+Ne_n clusters as a function of cluster size obtained at the $B3LYP/6-311 + + G(2d,2p)$ level of theory.

increases. This behavior can be attributed to the dominance of the Li^+Ne interaction, which is considerably stronger than that of the newly formed $Ne - Ne$ bonds. These variations align with the findings reported by Dhiflaoui et al.[78,81−83] for similar heterogeneous systems.[84]

Another important factor for examining cluster stability is the fragmentation energy, denoted as $E_f(n)$. Figure 5 illustrates the variation of fragmentation energies as a function of cluster size by using both the pairwise model and DFT methods. Notably, the curves obtained from both methods exhibit a similar trend. It can be observed that Li^+Ne_6 and Li^+Ne_{14} clusters display higher fragmentation energies compared to those of their neighboring clusters, indicating their heightened

stability. Consequently, these clusters are significantly resistant to fragmentation and exhibit lower reactivity.

The consideration of neighboring clusters, relative stability, is better accomplished by calculating second-order difference of energies $\Delta_2E(n)$. This quantity is very useful to identify the so-called "magic numbers" that are usually compared with experimental mass spectrum intensities. Figure 7 represent Δ_2E as a function of n. It is clear in this figure that high stability peaks arise at $n = 6$ for both the pairwise model and $DFT/$ $B3LYP$ method. Other less pronounced peaks that arise for larger clusters are $n = 8, 12, 14, 16,$ and 17 for pairwise model and 4, 6, 8, 10, 12, 14, and 16 for $DFT/B3LYP$. The special stability at $n = 6$ coincide with those observed by Froudakis et
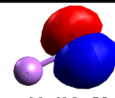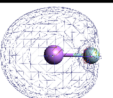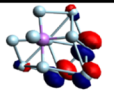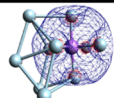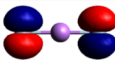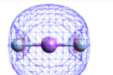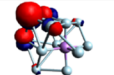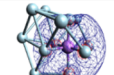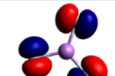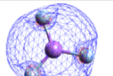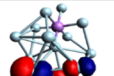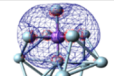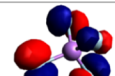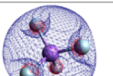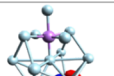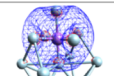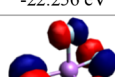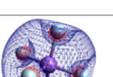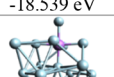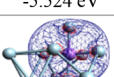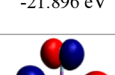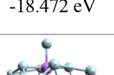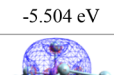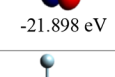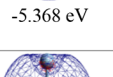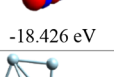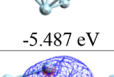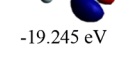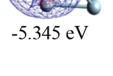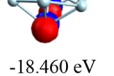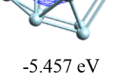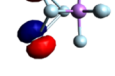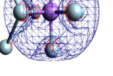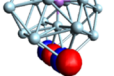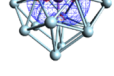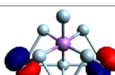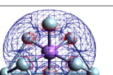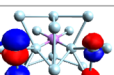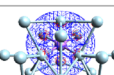
n	HOMO	LUMO	n	HOMO	LUMO
1	-22.628 eV	-6.928 eV	11	-19.044 eV	-5.414 eV
2	-22.607 eV	-6.609 eV	12	-18.564 eV	-5.541 eV
3	-22.426 eV	-6.326 eV	13	-18.564 eV	-5.393 eV
4	-22.256 eV	-6.022 eV	14	-18.539 eV	-5.524 eV
5	-21.896 eV	-5.768 eV	15	-18.472 eV	-5.504 eV
6	-21.898 eV	-5.368 eV	16	-18.426 eV	-5.487 eV
7	-19.245 eV	-5.345 eV	17	-18.460 eV	-5.457 eV
8	-19.533 eV	-5.483 eV	18	-18.429 eV	-5.426 eV
9	-19.475	-5.446 eV	19	-18.455 eV	-5.455 eV
10	-19.035 eV	-5.449 eV	20	-18.478 eV	-5.657 eV

Figure 8. HOMO and LUMO iso-surfaces diagrams of the Li^+Ne_n clusters obtained at the $B3LYP/6-311 + + G(2d,2p)$ level of theory.

al.[20] in their mass spectra experiments on Li^+Ne_n clusters. In their study, the authors refer also to the clusters for $n = 14$ and 16 as having particular stability. Although such peaks are also present for both pairwise model and $DFT/B3LYP$, they are not particularly prominent (e.g., Li^+Ne_8).

III.3. Dipolar and Electronic Properties. *a. Transition Dipole Moment.* To understand the interatomic interactions and study the electrostatic and optical properties of the Li^+Ne_n clusters, it is crucial to determine the dipolar properties. The DFT approach is considered as an interesting method for accurately determining these properties, unlike other quantum methods that face numerous challenges in this regard.[48] The dipole moment of the Li^+Ne_n complexes, as a function of cluster size, was computed by using the DFT method and is illustrated in Figure 7. It is evident from the figure that all Li^+Ne_n clusters exhibit a polar character, except for $n = 2, 3, 4, 5,$ and 6, which possess a very weak dipole moment close to zero. The Li^+Ne cluster exhibits the highest dipole moment ($\mu = 8.29$ D), and subsequently, the dipole moment fluctuates irregularly with the number of neon atoms. Clusters with a
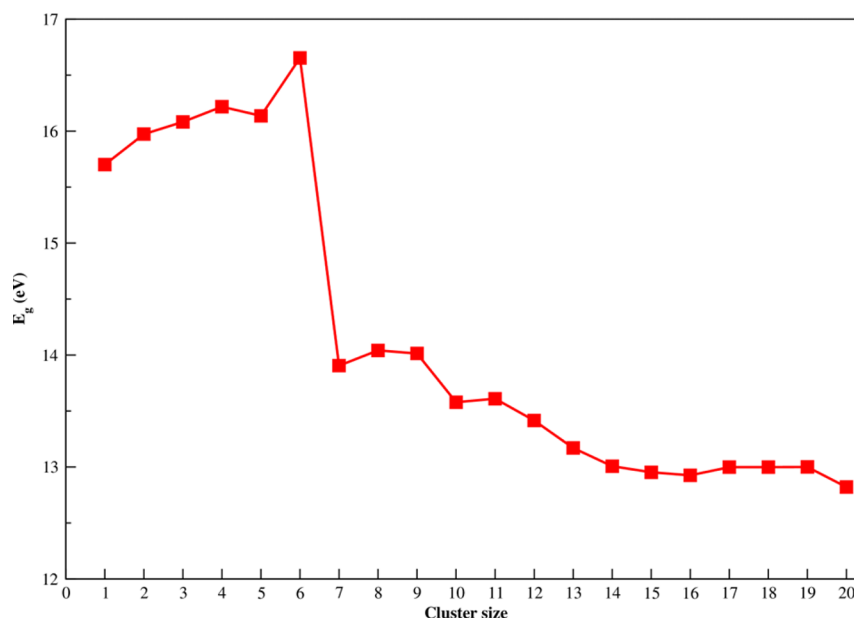
Figure 9. HOMO−LUMO gap (E_g) of Li^+Ne_n clusters obtained at the $B3LYP/6−311 + + G(2d,2p)$ level of theory.

large dipole moment display a high degree of charge separation.[48] Based on Figure 7, the Li^+Ne_6 cluster exhibits small values of dipole moment ($\mu = 4.1 10^{-4}$ Debye), indicating low charge separation due to its high stability.

b. Frontier Molecular Orbitals HOMO and LUMO. In order to understand the interaction processes occurring within Li^+Ne_n clusters, the HOMO (highest occupied molecular orbital) and LUMO (lowest unoccupied molecular orbital) energies were computed for the most stable clusters with n ranging from 1 to 20. The results are presented in Figure 8, where the blue and red colors represent the negative and positive regions, respectively. As can be seen from this figure, the LUMO energy is higher than the HOMO energy in van der Waals Li^+Ne_n clusters, which can be explained by the nature of the bonding in these systems. In addition, in a Li^+Ne_n cluster, the HOMO is the highest energy level that is occupied by electrons, while the LUMO is the lowest energy level that is unoccupied. Since the intermolecular interactions are weak, the energy required to remove an electron from the HOMO and promote it to the LUMO (creating a charged species) is relatively high.[86] Furthermore, in van der Waals clusters, the electrons are more delocalized compared with the corresponding LUMO orbitals. This delocalization leads to a lower energy for the HOMO orbital[87]

The size-dependence curves of HOMO−LUMO gaps of clusters Li^+Ne_n ($n = 1−20$) are shown in Figure 9. It can be observed that these gaps exhibit oscillating behavior, similar to the fragmentation energies and second-order difference of energies. Unlike covalent or ionic systems, weak intramolecular bonding in Li^+Ne_n clusters lead to wider energy gaps between the occupied and unoccupied orbitals. Specifically, the HOMO−LUMO gaps of the Li^+Ne_6 cluster are larger compared with neighboring clusters, indicating its superior chemical stability. This observation is consistent with the analysis based on the binding energies (e_b) of the Li^+Ne_6 clusters. Thus, the larger HOMO−LUMO gaps in the Li^+Ne_6 cluster imply a higher energy requirement for electron excitation and fragmentation, highlighting its heightened chemical stability.

III.4. Thermodynamic Properties. The thermodynamic properties of Li^+Ne_n ($n = 1−20$) clusters such as binding enthalpy (ΔH_b), binding entropy (ΔS_b), and Gibbs free energy (ΔG_b) were computed at 298.15 K. The calculated values of ΔH_b, ΔS_b and ΔG_b have been summarized in Table 4.

The binding enthalpy is computed from

$$\Delta H_b = E_c(Li^+Ne_n) - E_c(Li^+) - nE_c(Ne)$$

where $E_c(Li^+Ne_n)$, $E_c(Li^+)$, and $E_c(Ne)$ are the sum of electronic energy and thermal enthalpy correction of each Li^+Ne_n and Ne species.

Table 4. Calculated Binding Enthalpy (ΔH_b), Entropy (ΔS_b), Gibbs Free Energy (ΔG_b), and Variation of Thermal Enthalpy Correction (Δh_b) of Li+Ne$_n$ Clusters Obtained at the *DFT* Level and Theory

number of Ne atoms	ΔH_b (kcal mol^{-1})	Δh_b (kcal mol^{-1})	ΔS_b (kcal mol^{-1} K^{-1})	ΔG_b (kcal mol^{-1})
1	−6.02	0.39	−0.015	1.42
2	−6.51	0.27	−0.03	2.21
3	−10.13	0.27	−0.05	5.22
4	−12.94	0.81	−0.07	9.43
5	−15.08	1.27	−0.09	14.46
6	−17.30	1.79	−0.12	19.21
7	−15.47	2.22	−0.14	27.16
8	−15.62	2.72	−0.16	33.52
9	−15.78	3.19	−0.18	39.89
10	−16.30	2.73	−0.21	46.70
11	−15.86	4.16	−0.22	52.32
12	−13.66	4.62	−0.25	61.36
13	−13.49	5.10	−0.27	67.39
14	−15.33	2.79	−0.29	71.27
15	−13.73	6.07	−0.31	80.24
16	−14.41	5.56	−0.33	86.56
17	−13.92	7.00	−0.35	93.00
18	−15.23	5.59	−0.38	100.10
19	−16.08	2.58	−0.41	107.78
20	−13.46	2.30	−0.44	117.73

To find out if the formation reactions of Li^+Ne_n clusters from Li and Ne atoms is exothermic or not, we calculate Δh_b from

$$\Delta h_b = h(Ne_nLi^+) - h(Li^+) - nh(Ne)$$

where $h(Li^+Ne_n)$ is the thermal correction to enthalpy for Li^+Ne_n clusters. The values of Δh_b are collected in Table 4. We note from the table that the formation reactions of Li^+Ne_n clusters are endothermic processes for all sizes of the Li^+Ne_n cluster.

The binding entropy energy is calculated from

$$\Delta S_b = S(Li^+Ne_n) - S(Li^+) - nS(Ne)$$

where $S(Li^+Ne_n)$, $S(Li^+)$, and $S(Ne)$ are the entropy values of Li^+Ne_n, Li^+, and Ne species. From Table 4, ΔS_b values decrease with the increases in the cluster sizes. This shows that the Li^+Ne_n complexes have an ordered structure.

The binding ΔG_b Gibbs free energy is calculated from

$$\Delta G_b = \Delta H_b - T\Delta S_b$$

where T is the temperature in Kelvin ($T = 298.15$). It is noted that all ΔG_b values are positive for the Li^+Ne_n clusters, indicating the nonspontaneous nature of the formation process.

IV. CONCLUSIONS

In this study, we investigate the structure, stability, electronic, and thermodynamic properties of Li^+Ne_n, using both a pairwise additive potential model and the density functional theory (DFT). To determine the interactions between Li^+ and Ne, as well as the $Ne - Ne$ interactions within the pairwise model, ab initio calculations are performed using the $CCSD(T)$ method with the $aug - cc - pVn$ ($n = D, T, Q,5$, or 6) Z basis sets. The resulting energies are subsequently corrected using the CBS approach. Furthermore, the ab initio $CCSD(T)/CBS[Q5]$ and $CCSD(T)/aug - cc - pV6Z$ methods are utilized to fit the core−core Li^+Ne potential using the analytical form proposed by Tang and Toennies (TT), while the $Ne - Ne$ interaction is described by the Lennard-Jones (LJ) potential. Additionally, we incorporate the induced many-body effect (V_{3B}) to improve the description of the potential energy surface of Li^+Ne_n clusters. The potential energy surface of all clusters is explored using a basin-hopping method.

For all Li^+Ne_n ($n = 1-20$) clusters, we reoptimized these geometries by using the ab initio DFT method. The Li^+Ne_n clusters obtained from pairwise model potential had good agreement with the corresponding ones optimized at the DFT level. In contrast, the comparison between the two methods displays systematically the same structures with a small difference.

The stability of Li^+Ne_n clusters is evaluated based on several factors, including binding energy, fragmentation energy, second-order derivative energy, and the HOMO−LUMO energy gap. As a result, it is determined that the octahedral structure of Li^+Ne_6 represents the most stable cluster. Our results indicate the presence of clusters with a particularly stable icosahedral structure for $n = 4, 6, 8, 12, 14, 16,$ and 17 (the so-called "magic numbers"). These structures exhibited good agreement with the time-of-flight (TOF) experiments of Froudakis et al.[20] This comparison between theoretical and experimental results helps validate the accuracy of theoretical models and provides a means to refine and improve these

models. Additionally, the results demonstrate that all Li^+Ne_n clusters exhibit polar character.

Furthermore, thermodynamic properties such as binding enthalpy, entropy, and Gibbs free energy were calculated. These calculations indicate that the formation of Li^+Ne_n clusters is an endothermic process and is nonspontaneous in nature.

The geometric structure of the $Li^+−Ne_n$ clusters will be utilized for reduced density gradient analysis (RDG) in future studies.

■ ASSOCIATED CONTENT

Data Availability Statement

This declaration is not applicable

■ AUTHOR INFORMATION

Corresponding Authors

Jamila Dhiflaoui − *Laboratory of Interfaces and Advanced Materials, Physics Department, Faculty of Sciences of Monastir, Monastir 5019, Tunisia;* orcid.org/0000-0002-3827-3499; Email: jamila.dhiflaoui@ipeim.u-monastir.tn

Hamid Berriche − *Laboratory of Interfaces and Advanced Materials, Physics Department, Faculty of Sciences of Monastir, Monastir 5019, Tunisia; Mathematics and Physics Department, School of Arts and Sciences, American University of Ras Al Khaimah, Ras Al-Khaimah 10021, UAE;* orcid.org/0000-0002-1442-669X; Email: hamid.berriche@aurak.ac.ae

Authors

Nesrine Mabrouk − *Laboratory of Interfaces and Advanced Materials, Physics Department, Faculty of Sciences of Monastir, Monastir 5019, Tunisia*

Mohamed Bejaoui − *Laboratory of Interfaces and Advanced Materials, Physics Department, Faculty of Sciences of Monastir, Monastir 5019, Tunisia*

Samah Saidi − *Laboratory of Interfaces and Advanced Materials, Physics Department, Faculty of Sciences of Monastir, Monastir 5019, Tunisia; Department of Physics, College of Science and Humanities in Al-Kharj, Prince Sattam bin Abdulaziz University, Al-Kharj 16273, Saudi Arabia*

Complete contact information is available at:
https://pubs.acs.org/10.1021/acsomega.3c05238

Author Contributions

All authors have participated in calculations, analysis, and interpretation of the data; editing, reviewing, and improving the paper. All authors have read and agreed to the published version of the manuscript. This manuscript has not been submitted to, nor is under review at, another journal or other publishing venue.

Notes

The authors declare no competing financial interest.
This paper does not contain any studies with human participants or animals performed by any of the authors.

■ REFERENCES

(1) Shaw, A. M. *Astrochemistry: from Astronomy to Astrobiology*; John Wiley & Sons: Sussex (2006).

(2) Harrison, R. G.; Tammet, H. Ions in the Terrestrial Atmosphere and Other Solar System Atmospheres. *Space Sci. Rev.* **2008**, *137*, 107.

(3) Israël, H. *Atmospheric Electricity,* Vol. *I*, Israel Program for Sci. Transl. & NSF: Jerusalem, (1970).

(4) Luts, A.; Salm, J. Chemical composition of small atmospheric ions near the ground. *J. Geophys. Res.* **2004**, *99*, 10781.

(5) Beig, G.; Brasseur, G. P. Model of tropospheric ion composition: A first attempt. *J. Geophys. Res.* **2000**, *2000* (105), 22671.

(6) Curtius, J.; Lovejoy, E. R.; Froyd, K. D. Atmospheric Ion-induced Aerosol Nucleation. *Space Sci. Rev.* **2007**, *125*, 159.

(7) Yu, F.; Atmos. From molecular clusters to nanoparticles: second-generation ion-mediated nucleation model. *Chem. Phys.* **2006**, *2006* (6), 5193.

(8) Kazil, J.; Harrison, R. G.; Lovejoy, E. R. Tropospheric New Particle Formation and the Role of Ions. *Space Sci. Rev.* **2008**, *2008* (137), 241.

(9) Arnold, F. Atmospheric Ions and Aerosol Formation. *Space Sci. Rev.* **2008**, *2008* (137), 225.

(10) Shoji, F.; Feng, Z. B.; Kono, A.; Nagai, T. Spherical carbon particle growth in a methane plasma. *Appl. Phys. Lett.* **2006**, *2006* (89), 171504.

(11) Nagai, T.; Feng, Z. B.; Kono, A.; Shoji, F. Growth mechanism for spherical carbon particles in a dc methane plasma. *Phys. Plasmas* **2008**, *15* (5), No. 050702.

(12) Swindells, I.; Voronin, S. A.; Fotea, C.; Alexander, M. R.; Bradley, J. W. Detection of Negative Molecular Ions in Acrylic Acid Plasma: Some Implications for Polymerization Mechanisms. *J. Phys. Chem. B* **2007**, *2007* (111), 8720.

(13) Fujii, T. A novel method for detection of radical species in the gas phase: usage of Li+ ion attachment to chemical species. *Chem. Phys. Lett.* **1992**, *1992* (191), 162.

(14) Okumura, H.; Furuya, K.; Harata, A. Growth of fluorocarbon macromolecules in the gas phase: IV. Li+-attachment mass spectrometric investigation of high-mass neutral radicals in the downstream region of Ar/c-C4F8 plasmas. *J. Phys. D: Appl. Phys.* **2009**, *42*, No. 065205.

(15) Bellert, D.; Breckenridge, W. H. Bonding in Ground-State and Excited-State A+·Rg van der Waals Ions (A = Atom, Rg = Rare-Gas Atom): A Model-Potential Analysis. *Chem. Rev.* **2002**, *2002* (102), 1595−1622.

(16) Beyer, M. K. Hydrated metal ions in the gas phase. *Mass. Spectrom. Rev.* **2007**, *2007* (26), 517.

(17) Grandinetti, F. Gas-Phase Ion Chemistry of the Noble Gases: Recent Advances and Future Perspectives. *Eur. J. Mass Spectrom.* **2011**, *2011* (17), 423−463.

(18) Lüder, C.; Prekas, D.; Velegrakis, M. Ion-size effects in the growth sequences of metal ion doped noble gas clusters. *Laser. Chem.* **1997**, *17*, 109−122.

(19) Prekas, D.; Lüder, C.; Velegrakis, M. Structural transitions in metal ion-doped noble gas clusters: experiments and molecular dynamics simulations. *J. Chem. Phys.* **1998**, *108*, 4450−4459.

(20) Froudakis, G. E.; Farantos, S. C.; Velegrakis, M. Mass spectra and theoretical modeling of Li+Ne$_n$, Li+Ar$_n$ and Li+Kr$_n$ clusters. *J. Chem. Phys.* **2000**, *258*, 13−20.

(21) Ryan, M.; Collier, M.; Pujo, P.; Crépin, C.; Mc, J. G.; Caffrey. Investigations of the optical spectroscopy of atomic sodium isolated in solid argon and krypton: Experiments and Simulations. *J. Phys. Chem. A* **2010**, *114*, 3011−3024.

(22) Velegrakis, M.; Froudakis, G. E.; Farantos, S. C. Stability and structure of Ni+Ar$_n$ and Pt+Ar$_n$ clusters. *J. Chem. Phys.* **1998**, *109*, 4687−4688.

(23) Velegrakis, M.; Lüder, C. Formation and stability of singly and doubly charged MgAr$_n$ clusters. *Chem. Phys. Lett.* **1994**, *223*, 139−142.

(24) Wright, T. G.; Breckenridge, W. H. Radii of atomic ions determined from diatomic ion−He Bond Lengths. *J. Phys. Chem. A* **2010**, *114*, 3182−3189.

(25) Whetten, R. L.; Schriver, K. E.; Persson, J. L.; Hahn, M. Y. Photoionization and excitation energies of an Al atom in Ar N clusters. *J. Chem. Soc. Faraday. Trans.* **1990**, *86*, 2375.

(26) Farges, J.; de Feraudy, M. F.; Raoult, B.; Torchet, G. Noncrystalline structure of argon clusters. I. Polyicosahedral structure of Ar$_n$ clusters, 20 < n < 50. *J. Chem. Phys.* **1983**, *78*, 5067−5080.

(27) Farges, J.; de Feraudy, M. F.; Raoult, B.; Torchet, G. Noncrystalline structure of argon clusters. II. Multilayer icosahedral structure of Ar$_n$ clusters 50 < n < 750. *J. Chem. Phys.* **1986**, *84*, 3491−3501.

(28) Tsoo, C.; Estrin, D.; Singer, S. Electronic energy shifts of a sodium atom in argon clusters by simulated annealing. *J. Chem. Phys.* **1990**, *93*, 7187−7200.

(29) Maclyn, J.; Mc, M.; Carty; Robinson, G. W. Environmental perturbations on foreign atoms and molecules in solid argon, krypton and xenon. *Mol. Phys.* **1959**, *2*, 415−430.

(30) Meyer, B. Absorption Spectrum of Na and K in Rare Gas Matrices. *J. Chem. Phys.* **1965**, *43*, 2986−2992.

(31) Balling, L. C.; Havey, M. D.; Dawson, J. F. Absorption and emission spectra of Na atoms trapped in rare gas matrices. *J. Chem. Phys.* **1978**, *69*, 1670−1675.

(32) Balling, L. C.; Dawson, J. F.; Havey, M. D. Optical pumping between Levels of a Bistable state of Alkali Atoms trapped in Rare-Gas matrices. *J. Phys. Rev. Lett.* **1979**, *43*, 435−438.

(33) Wright, J. J.; Balling, L. C. Absorption and emission spectra of Na atoms trapped in a Ne matrix. *J. Chem. Phys.* **1978**, *73* (2), 994−996.

(34) Balling, L. C.; Wright, J. J. Use of dimer potentials to calculate the energy levels of alkali atoms in rare gas matrices. *J. Chem. Phys.* **1983**, *79*, 2941−2944.

(35) Balling, L. C.; Wright, J. J. Computer simulation of site formation for Na atoms trapped in Ar and Xe solids. *J. Chem. Phys.* **1984**, *81* (2), 675−679.

(36) Boatz, J. A.; Fajardo, M. E. Monte Carlo simulations of the structures and optical absorption spectra of Na atoms in Ar clusters, surfaces, and solids. *J. Chem. Phys.* **1994**, *101*, 3472−3487.

(37) Martyna, G.; Cheng, C.; Klein, M. L. Electronic states and dynamical behavior of LiXe$_n$ and CsXe$_n$ clusters. *J. Chem. Phys.* **1991**, *95*, 1318−1336.

(38) Prudente, F. V.; Marques, J. M. C.; Pereira, F. B. Solvation of Li$^+$ by argon: How important are three body forces. *Phys. Chem. Chem. Phys.* **2017**, *19*, 25707−25716.

(39) Lan, Y.-Z.; Feng, Y.-L. Comparative study on the geometric and energetic properties, absorption spectra, and polarizabilities of charged and neutral Cu@Sin clusters (n = 9−14). *Phys. Rev. A* **2009**, *79*, No. 033201.

(40) Gueorguiev, G. K.; Pacheco, J. M.; Stafström, S.; Hultman, L. Silicon−metal clusters: Nano templates for cluster assembled materials. *Thin Solid. Films.* **2006**, *515*, 1192−1196.

(41) Lin, L.; Yang, J. Small copper-doped silicon clusters CuSi$_n$ (n = 4−10) and their anions: structures, thermochemistry, and electron affinities. *J. Mol. Model.* **2015**, *21*, 155.

(42) Shi, S.; Liu, Y.; Zhang, C.; Denga, B.; Jiang, G. A. A computational investigation of aluminum-doped germanium clusters by density functional theory study. *Comput. Theor. Chem.* **2015**, *1054*, 8−15.

(43) Bhattacharjee, D.; Mishra, B. K.; Deka, R. C. A DFT study on structure, stabilities and electronic properties of double magnesium doped gold clusters. *RSC. Adv.* **2014**, *4*, 56571−56581.

(44) Li, Z.; Zhao, Z. Structures, stability, magnetic moments and growth strategies of the Fe$_n$N (n = 1−7) clusters: All-electron density functional theory calculations. *Mater. Chem. Phys.* **2017**, *187*, 54−59.

(45) LI, G.; MA, W.; GAO, A.; CHEN, H.; FINLOW, D.; LI, Q.-S. Density Functional Theory Studies of Charged, Copper-Doped, Small Silicon Clusters Cu$^+$Si$_n$. *J. Theor. Comput. Chem.* **2012**, *11*, 185−196.

(46) Ma, Q.-M.; Xie, Z.; Wang, B.-R.; Liu, Y.; Li, Y.-C. Structure, stability and magnetic moments of the Fe$_n$Cr clusters: All-electron density functional theory investigations. *Solid. State. Commun.* **2011**, *151*, 806−810.

(47) Marinetti, F.; Coccia, E.; Bodo, E.; Gianturco, F. A.; Yurtsever, E.; Yurtsever, M.; Yildirim, E. Bosonic helium clusters doped by alkali metal cations: interaction forces and analysis of their most stable structures. *Theor. Chem. Acc.* **2007**, *118*, 53−65.

(48) Ayed, M. Ben Hadj; Osmani, T.; Issaoui, N.; Berisha, A.; Oujia, B.; Ghalla, H. Structures and relative stabilities of Na$^+$Ne$_n$ (n = 1−16) clusters via pairwise and DFT calculations. *Theor. Chem. Acc.* **2019**, *138*, 84.

(49) Laajimi, M.; Mtiri, S.; Ghalla, H. Structure and stability of sodium-doped helium snowballs through DFT calculations. *Theor. Chem. Acc.* **2020**, *139*, 40.

(50) Mtiri, S.; Laajimi, M.; Ghalla, H.; Oujia, B. Microsolvation of Ca$_2^+$ cation in small Xe$_n$ clusters: Structures and relative stabilities. *Phys. B: Phys. Condens. Matter.* **2019**, *41*, 1849.

(51) Čížek, J. On the correlation problem in atomic and molecular systems. Calculation of wave function components in Ursell type expansion using quantum field theoretical methods. *J. Chem. Phys.* **1966**, *45*, 4256−4266.

(52) Čížek, J. On the use of the cluster expansion and the technique of diagrams in calculations of correlation effects in atoms and molecules. *Adv. Chem. Phys.* **1969**, *14*, 35−89.

(53) Bauschlicher, C. W.; Ranghoff, S. R.; Taylor, P. R.; Handy, N. C.; Knowles, P. J. Benchmark full configuration-interaction calculations on HF and NH$_2$. *J. Chem. Phys.* **1986**, *85*, 1469.

(54) Bauschlicher, C. W.; Taylor, P. R. Benchmark full configuration-interaction calculations on HaOF and F-. *J. Chem. Phys.* **1986**, *85*, 2779.

(55) Davidson, E. R. Electronic Population Analysis of Molecular Wave functions. *J. Chem. Phys.* **1967**, *46*, 3320.

(56) Dunning, T. H., Jr Gaussian basis sets for use in correlated molecular calculations. I. The atoms boron through neon and hydrogen. *J. Chem. Phys.* **1989**, *90*, 1007.

(57) Peterson, K. A.; Woon, D. E.; Dunning, T. H., Jr Benchmark calculations with correlated molecular wave functions. IV. The classical barrier height of the H+H$_2$→H$_2$+H reaction. *J. Chem. Phys.* **1994**, *100*, 7410.

(58) Feller, D.; Sordo, J. A. A CCSDT study of the effects of higher order correlation on spectroscopic constants. I. First row diatomic hydrides. *J. Chem. Phys.* **2000**, *112*, 5604.

(59) Schwartz, C. Importance of Angular Correlations between Atomic Electrons. *Phys. Rev.* **1962**, *126*, 1015.

(60) Werner, H. J.; Knowles, P. J.; Knizia, G.; Manby, F. R.; Schütz, M. *MOLPRO version 2010.1, a package of ab-initio programs.* http://www.molpro.net. **2010**.

(61) Viehland, L. A. Interaction potentials for Li$^+$-rare-gas systems. *Chem. Phys.* **1983**, *78*, 279−294.

(62) Roeggen, I.; Skullerud, H. R. The interatomic potential for the X^{1}Sigma state of NeLi$^+$. *J. Phys. B: At. Mol. Opt. Phys.* **1992**, *25*, 1795.

(63) Soldán, P.; Lee, E. P.; Lozeille, J.; Murrell, J. N.; Wright, T. G. High-quality interatomic potential for Li$^+$He. *Chem. Phys. Lett.* **2001**, *343*, 429−436.

(64) Røggen, I.; Skullerud, H. R. The interatomic potential for the X$^1\Sigma^+$ state of NeLi$^+$. *J. Phys. B: At. Mol. Opt. Phys.* **1992**, *25*, 1795.

(65) Pirani, F.; Brizi, S.; Roncaratti, L. F.; Casavecchia, P.; Cappelletti, D.; Vecchiocattivi, F. Beyond the lennard-jones model: A simple and accurate potential function probed by high resolution scattering data useful for molecular dynamics simulations. *Phys. Chem. Chem. Phys. PCCP* **2008**, *10*, 5489−503.

(66) Yang, C. L.; Zhang, X.; Han, K. L. Theoretical study on analytical potential function and spectroscopic parameters for CaF molecule. *J. Mol. Struct. (THEOCHEM)* **2004**, *678*, 183−188.

(67) Standard, J. M.; Certain, P. R. Bounds to two and three body long range interaction coefficients for S state atoms. *J. Chem. Phys.* **1985**, *83*, 3002−3008.

(68) Tang, K. T.; Toennies, J. Peter An improved simple model for the van der Waals potential based on universal damping functions for the dispersion coefficients. *J. Chem. Phys.* **1984**, *80*, 3726.

(69) Schwerdtfeger, P.; Gaston, N.; Krawczyk, R. P.; Tonner, R.; Tonner, R.; Moyano, G. E. Extension of the Lennard-Jones potential: Theoretical investigations into rare-gas clusters and crystal lattices of He, Ne, Ar, and Kr using many-body interaction expansions. *Phys. Rev. B* **2006**, *73*, No. 064112.

(70) Zanuttini, D.; Jacquet, E.; Giglio, E.; Douady, J.; Gervais, B. An accurate model potential for alkali neon systems. *J. Chem. Phys.* **2009**, *131*, 214104.

(71) Jones, J. E.; Ingham, A. E. On the Calculation of Certain Crystal Potential Constants, and on the Cubic Crystal of Least Potential Energy. *Proc. Math. Phys. Eng. Sci.* **1925**, *107*, 636−653.

(72) Yang, C. L.; Zhang, X.; Han, K. L. Theoretical study on analytical potential function and spectroscopic parameters for CaF molecule. *J. Mol. Struct.* **2004**, *678*, 183−188.

(73) Standard, J. M.; Certain, P. R. Bounds to two and three body long range interaction coefficients for S state atoms. *J. Chem. Phys.* **1985**, *83*, 3002−3008.

(74) Rastogi, M.; Leidlmair, C.; An der Lan, L.; Ortiz de Zárate, J.; Pérez de Tudela, R.; Bartolomei, M.; Hernandez, M. I.; Campos-Martínez, J.; González-Lezana, T.; Hernández-Rojas, J.; Bretón, J.; Scheier, P.; Gatchell, M. Lithium ions solvated in helium. *Phys. Chem. Chem. Phys.* **2018**, *20*, 25569−25576.

(75) Doye, J. P. K.; Wales, D. J. On potential energy surfaces and relaxation to the global minimum. *J. Chem. Phys.* **1996**, *105*, 8428−8445.

(76) Ramírez, R.; Herrero, C. P. Quantum path-integral study of the phase diagram and isotope effects of neon. *J. Chem. Phys.* **2008**, *129*, 204502.

(77) Calvo, F.; Yurtsever, E. Composition-induced structural transitions in mixed rare-gas clusters. *Phys. Rev. B* **2004**, *70*, No. 045423.

(78) Al-Ahmari, M.; Saidi, S.; Dhiflaoui, J.; Hassen, F.; Berriche, H. Structure and Stability of the Li$^+$Xe$_n$ and LiXe$_n$ Clusters. *J. Clust. Sci.* **2015**, *26*, 913−924.

(79) Frisch, M. J.; Trucks, G. W.; Schlegel, H. B.; Gill, P. M. W.; Johnson, B. G.; Robb, M. A.; Cheeseman, J. R.; et al.et al *GAUSSIAN 94 GAUSSIAN 94*, Revision D.4.; Gaussian Inc.: Pittsburgh, PA, 1995.

(80) Temelso, B.; Mabey, J. M.; Kubota, T.; Appiah-Padi, N.; Shields, G. C. ArbAlign: A Tool for Optimal Alignment of Arbitrarily Ordered Isomers Using the Kuhn−Munkres Algorithm. *J. Chem. Inf. Model.* **2017**, *57* (5), 1045−1054.

(81) Dhiflaoui, J.; Berriche, H. Stability and structure of the Rb$^+$Ar$_n$ (n = 1−20) small clusters. *Int. J. Nanoparticles.* **2009**, *2*, 1−6.

(82) Dhiflaoui, J.; Bouzouita, H.; Berriche, H. Theoretical study of the Na$^+$Kr$_n$ and NaKr$_n$ (n = 1−25) small clusters. *Phys. Procedia.* **2009**, *2*, 1175.

(83) Dhiflaoui, J.; Bouzouita, H.; Berriche, H. Stability and Structure of Na$^+$Kr$_n$(n = 1−20)Clusters. *AIP Conf. Proc.* **2007**, *963*, 19−22.

(84) Issaoui, N.; Ghalla, H.; Muthu, S.; Flakus, H. T.; Oujia, B. Molecular structure, vibrational spectra, AIM, HOMO−LUMO, NBO, UV, first order hyperpolarizability, analysis of 3-thiophene-carboxylic acid monomer and dimer by Hartree−Fock and density functional theory. *Spectrochim. Acta A* **2015**, *136*, 1227−1242.

(85) Ahlrichs, R.; Böhm, H. J.; Brode, S.; Tang, K. T.; Toennies, J. P. Interaction potentials for alkali ion−rare gas and halogen ion−rare gas systems. *J. Chern. Phys.* **1988**, *88* (10), 6290−6302.

(86) Pitriana, P.; Wungu, T. D. K.; Herman, H.; Hidayat, R. Electronic Structure Calculations of Alkali Lead Iodide APbI3 (A = Li, Na, K, Rb or Cs) using Density Functional Theory (DFT) Method. *J. Phys.: Conf. Series* **2019**, *1204*, No. 012107.

(87) Kimber, P.; Plasser, F. Energy Component Analysis for Electronically Excited States of Molecules: Why the Lowest Excited State Is Not Always the HOMO/LUMO Transition. *J. Chem. Theory Comput.* **2023**, *19* (8), 2340−2352.